AIAA AVIATION Forum
June 25-29, 2018, Atlanta, Georgia
2018 Fluid Dynamics Conference

10.2514/6.2018-3712

Turbulent Hypersonic Flow Effects on Optical Sensor Performance

Lauren E. Mackey,[1] and Iain D. Boyd.[2]
Department of Aerospace Engineering, University of Michigan, Ann Arbor, MI

Joseph S. Jewell,[3] and Timothy J. Leger.[4]
U.S. Air Force Research Laboratory, Wright-Patterson Air Force Base, OH 45433

Abstract

If an optical signal were to travel through a hypersonic flowfield, the type of high-speed flow analysis required to perform reliable assessments of sensor performance is unclear. In the present study, numerical simulations are utilized to perform implicit large eddy computations of a Mach 4 flow over an adiabatic flat plate. The simulations are run with and without thermochemistry models to determine the effects thermochemical nonequilibrium has on optical distortion. The higher fidelity simulation method of accounting for thermochemical nonequilibrium produces less variation in optical path difference (OPD) across the sensor aperture. The root mean square average of OPD is significantly smaller for the real gas simulation when compared to a perfect gas. These differences in OPD occur because nonequilibrium energy exchanges act to damp out turbulent fluctuations. It is, therefore, necessary to include these physical flow effects in optical assessments to obtain an accurate description of the aero-optic distortions.

I. Nomenclature

OPD	=	Optical Path Difference [m]
OPL	=	Optical Path Length [m]
t	=	Time [s]
Ψ	=	Stream Function
$\dot{\omega}$	=	Source Terms
τ_s	=	Relaxation Time [s]
τ_{rk}	=	Interspecies Relaxation Time [s]
M	=	Mach Number
n	=	Index of refraction
T	=	Temperature [K]
p	=	Pressure [kPa]
ρ	=	Density [kg/m^3]
K_{GD}	=	Gladstone-Dale constant [m^3/kg]
K_s	=	Individual species Gladstone-Dale constant [m^3/kg]
l	=	Coordinate along line of sight [m]
u_s	=	Diffusion Velocity [m/s]
K_{EQ}	=	Equilibrium rate Coefficient
k_f	=	Forward rate Coefficient
k_b	=	Backward rate Coefficient
k	=	Thermal Conductivity [W/(m·K)]

[1] Ph.D. Candidate, AIAA Student Member.
[2] James E. Knott Professor of Engineering, AIAA Fellow.
[3] Research Scientist, Spectral Energies, LLC, AFRL/RQHF, AIAA Senior Member.
[4] Research Scientist, Ohio Aerospace Institute, AFRL/RQHF, AIAA Senior Member.

θ = Characteristic Temperature [K]

Subscripts

∞ = Free stream
‘ = Fluctuating
s = Species
v = Vibrational
* = Equilibrium
<> = Spatial Mean
d = Dissociation
trans = Translational
c = Controlling

II. Introduction

As technology advances, flight in the hypersonic regime is becoming more tenable. To accurately assess signal propagation through the media surrounding a hypersonic vehicle, turbulent high enthalpy flow physics may need to be incorporated into evaluation of optical sensor performance.

High enthalpy effects in high gradient regions (such as boundary layers) may need to be addressed in the optical assessments. When the flow passes through these high gradient regions, it takes a finite number of molecular collisions for the internal energies to adjust to a new thermodynamic state, often resulting in regions of thermal nonequilibrium. Vibrational relaxation processes are often relatively slow (compared to translation and rotation) to adjust to rapidly changing flow fields.

In thermal nonequilibrium regions, dissociation can be significant when the Mach number exceeds 6. Dissociation depends on the state of the energy modes and consequently their relaxation processes. All of these combined thermochemical nonequilibrium processes affect optical properties because as an optical beam traverses a nonequilibrium flow field, it will encounter varying densities of the atomic and molecular species. Each of these species has distinct optical properties that need to be considered.

Modeling turbulent effects also may be essential to the assessment of the flowfield surrounding a hypersonic air vehicle. These vehicles would most likely operate in the turbulent regime. Turbulence is characterized by fluctuations in the bulk flow quantities, such as total and species densities. These fluctuations can further disrupt beam propagation, as index of refraction is proportional to these densities.[1]

Studies that investigate the interaction between turbulence and chemical reactions are scarce. The few studies that do exist have shown that turbulence may exert a significant effect on detailed chemical composition.[2] Furthermore, these studies show that exothermic reactions increase turbulent fluctuations and endothermic reactions dampen turbulent fluctuations. In the boundary layer, both types of reactions are possible, as species may dissociate and recombine. It should be noted that these past studies neglected thermal nonequilibrium.

There are a small number of studies that involve only thermal nonequilibrium in turbulent flow.[5,20-24] The existing studies impose varied relaxation times and draw conclusions depending on these preselected times. Perhaps most useful to the present study, the thermal nonequilibrium studies found that if the vibrational energy lags behind the other energy modes, energy will be transferred out of the other modes (e.g. turbulent kinetic energy) into the vibrational mode.[3] Consequently, the turbulent fluctuations can be damped. The interplay between turbulence, chemistry, and vibrational relaxation can affect the flow around a hypersonic vehicle and consequently the optical properties of that flow.

Even fewer studies have investigated a turbulent flow in thermochemical nonequilibrium to calculate optical properties.[5,20-24] Most studies focus on low enthalpy perfect gas flows. The published data reflect the consideration of only perfect air as the mixture for calculating the optical properties.[5,20-24] The flow media surrounding a hypersonic vehicle cannot be accurately represented by a perfect gas.

The investigation described in this paper consists of two turbulent Mach 4 flows over a flat plate. These computations are performed using implicit large eddy simulation (ILES). While Mach 4 is not in the traditional hypersonic regime, flow conditions are such that they induce nonequilibrium and turbulent effects. Conditions are representative of post-shock conditions for a 26 degree wedge flying at Mach 20 at 20 km in altitude.[2,3] One case is run utilizing thermochemical nonequilibrium models and the other utilizes a calorically perfect gas model. The perfect gas case provides a comparison for the nonequilibrium simulation and has internal energy only in the equilibrated translational and rotational modes. The optical calculations are performed on each set of flowfield data

and the differences are quantified. The optical calculations are carried out as a post processing step for both cases using the Gladstone-Dale relation.[1] During this post-processing routine, a separate grid is created for the optical calculations and the appropriate integrations are conducted along the signal propagation path.

This paper first presents the numerical methods employed for the mean flow (for both perfect and real gas) and details the optical calculations (for perfect and real gas). The simulation setup is then presented. The next section presents and discusses the results. The final section of the paper discusses the conclusions regarding the optical calculations performed on the perfect and real gas flows. The final section also describes future work.

III. Analysis

The analysis is described in two sections: (1) computational analysis of the flow field around the body of interest including the nonequilibrium models used in this study, and (2) optical assessments, for both real and perfect gases.

A. Flow Field Calculations

This study is conducted using the finite volume US3D code, a computational fluid dynamics code for high speed flows that was developed at the University of Minnesota.[6] US3D couples the Navier-Stokes equations with thermodynamic and transport property models. US3D utilizes finite rate chemistry and energy relaxation models as described in section III B.

In US3D, the viscous terms are calculated using a 2nd order central scheme. The inviscid terms are calculated using a 6th order central scheme.[7] The time integration is performed using a 2nd order implicit method. The turbulence studies can be conducted because of the low dissipation schemes US3D utilizes. The high order terms are used to help reduce the number of grid points required in the computational domain to resolve the turbulence.

The US3D simulations are run using an implicit filter. An implicit LES method does not resolve the smallest flow features. Instead, it relies on the grid to act as the filter. All features that are not resolved will be numerically dissipated. This level of resolution is acceptable for an optical study because the most optically important features are approximately the size of the boundary layer.[7]

In the present study, turbulence on the flat plate is induced by imposing alternating pairs of counter-rotating vortices. These disturbances are imposed on a laminar boundary layer at an inflow plane, and they create both down and up-wash flow features.[7] The flow's up and down wash features are developed from the stream function, Eqn. (1).

$$\Psi = AU_\infty \bar{x}\bar{y}^3\bar{z}\exp(-\bar{x}^2 - \bar{y}^2 - \bar{z}^2) \tag{1}$$

where

$$u' = 0 \qquad v' = -\frac{\partial \Psi}{\partial z} \qquad w' = \frac{\partial \Psi}{\partial y} \tag{2}$$

$\bar{x}, \bar{y}, \bar{z}$ are coordinates scaled with the characteristic lengths of the vortex disturbance, and A is the strength of the vortices. A is a fraction of freestream velocity and is chosen to be 0.1 for the cases described in this study. These vortical disturbances are imposed on a laminar solution for a flow with the same free stream parameters at 0.3 m from the leading edge. The original laminar solutions, both real and perfect, are produced by the NASA Data Parallel-Line Relaxation (DPLR) code[26], which has been used successfully to compute both real [27,] and perfect gas [28,] laminar boundary layers for instability and transition modeling.

Thermochemical Non-Equilibrium Modeling

US3D uses the Landau Teller Relaxation model to describes vibrational-translational energy coupling; see Eqn. (3):[13]

$$\dot{\omega_v} = \rho_s \frac{(e_{v_s}^* - e_{v_s})}{\tau_r} \tag{3}$$

where $\dot{\omega_v}$ is the energy exchange rate for the vibrational mode, e_v^*, s is the equilibrium vibrational energy of species s at the local translational temperature, and $e_{v,s}$ is the vibrational energy of each molecular species. The relaxation time can be found using Eqn. (4).[13]

$$\tau_s = \frac{\sum_s X_s}{\sum_s X_s/\tau_{rs}} \tag{4}$$

where X_s is the mole fraction of the species *s*. The inter-species relaxation time, τ_{rs} , is found using the Millikan and White approximation; see Eqn. (5).[14]

$$p\tau_{rs} = (-18.42) + (1.16 \times 10^{-3})\mu^{\frac{1}{2}}\theta_v^{\frac{4}{3}}\left(T^{-\frac{1}{3}} - 0.01\mu^{\frac{1}{4}}\right) \qquad atm \cdot s \tag{5}$$

For a simple harmonic oscillator, the vibrational temperature for each species can be found with a known vibrational energy and Eqn. (6).

$$e_v = \frac{R\theta_{v,s}}{exp\,(\frac{\theta_{v,s}}{T_v}) - 1} \tag{6}$$

where R is the species gas constant and θ_{vs} is the characteristic temperature of vibration for each species, s.

For the real gas simulation, the chemical source terms for the conservation of mass species are found utilizing the law of mass action and 17 reactions that occur with the 5 primary species in dissociating air (N_2, O_2, NO, N, and O); see Eqn. (7) for the 17 reactions. In Eqn. (7) M is representative of all 5 collisional partners.

$$\begin{gathered} N_2 + M \leftrightarrow 2N + M \quad (i) \\ O_2 + M \leftrightarrow 2O + M \quad (ii) \\ NO + M \leftrightarrow N + O + M \quad (iii) \\ NO + O \leftrightarrow O_2 + N \quad (iv) \\ N_2 + O \leftrightarrow NO + N \quad (v) \end{gathered} \tag{7}$$

The first three sub-equations (*i-iii*) in Eqn. (7) represent the dissociation and recombination of N_2, O_2, and NO, respectively. The last two reactions in Eqn. (7) are exchange reactions involving NO. In equilibrium, oxygen begins to dissociate at approximately 2000 K, followed by nitrogen at about 4000 K. NO forms at approximately 2000 K through dissociated O atoms colliding with the abundant N_2 molecules (via Eq. (7 *v*)).[8] NO will begin to dissociate at higher temperatures than O_2.[9] The expressions used for the forward reaction rate and backward reaction rate are shown in Eqns. (8) and (9), respectively. The constants and reaction rates are taken from Park.[10]

$$k_f(T_c) = C_f T_c^{\eta} exp\,(\frac{\theta_d}{T_c}) \tag{8}$$

$$k_b(T_c) = \frac{k_f}{K_{eq}} \tag{9}$$

where K_{eq} is the equilibrium rate coefficient and T_c is the controlling temperature; see Eqn.(10). Using T_c allows one to account for the effect of vibrational relaxation on chemical dissociation.[11]

$$T_c = \sqrt{TT_v} \tag{10}$$

where T is the translational temperature and T_v is the vibrational temperature. This model is referred to as Park's two- temperature model.[12]

B. Optical Assessments

Optical assessment of an initially planar wave front begins with obtaining the index of refraction of the medium, i.e., the air around the vehicle. The index of refraction can be found from the density profile using the Gladstone-Dale relation as follows:[1]

$$n = K_{GD}\rho + 1 \tag{11}$$

where *n* is the index of refraction, ρ is density and K_{GD} is the Gladstone-Dale constant. In the perfect gas studies, it is assumed that the Gladstone-Dale constant is unchanging and can be found using the equilibrium concentrations of the 5 component species in 5000 K air. However, in the real gas simulations, the effects of thermochemical nonequilibrium are included, and thus the Gladstone-Dale constant may change throughout the flowfield and is found in the following manner:[1]

$$K_{GD} = \sum K_s\left(\frac{\rho_s}{\rho}\right) \tag{12}$$

where K_s is the Gladstone-Dale constant for each species, ρ_s is the species density, and ρ is the total density. The experimentally obtained Gladstone-Dale constants for each species are listed in Table 1.[5,6,37]

Table 1. Species' Gladstone-Dale Constants at 5 μm[15,16,17]

Species	Gladstone-Dale Constant
N_2	2.40 x10^{-4} m^3/kg
N	3.10 x10^{-4} m^3/kg
O_2	1.93 x10^{-4} m^3/kg
O	2.04 x10^{-4} m^3/kg
NO	2.21 x10^{-4} m^3/kg

From Ref. 15, it was determined that in the temperature regimes that the experiments were performed, the Gladstone-Dale constants were largely independent of temperature. It was further suggested that since the Gladstone-Dale constant is a function of polarizability, for non-polar molecules and atoms the applicability of the calculated Gladstone-Dale constant extends beyond the range of experimentation.[15] NO, however, is a polar molecule and therefore its polarizability does depend on its thermal state. However, it was experimentally determined that the Gladstone-Dale constant for NO remained approximately constant in experiments involving Mach numbers exceeding 22.[15] Previous computations have used the Gladstone-Dale constant in Table 1 for NO for temperatures higher than 9000 K.

Once the index of refraction is known, it is possible to find the optical path length (OPL). This value is the product of the geometric distance a wave travels and the index of refraction. It can be thought of as the distance a wave front would travel in a vacuum in the same time it takes the wave front to traverse the geometric distance of interest.[18] When the index of refraction varies spatially as it does in this study, OPL is found as follows:

$$OPL = \int n(l)dl \tag{13}$$

The difference in optical path length between a portion of the wave front and a reference value, usually taken to be the spatially averaged OPL, is often of more interest in considering optical aberrations. This difference, referred to as optical path difference (OPD), is found using the following equation and is the chosen method for assessing optical distortion in this study:

$$OPD = OPL - < OPL > \tag{14}$$

OPD indicates how much the OPL departs from the mean value across the sensor aperture.[18]

The integral in Eq. (13) is evaluated by creating a mesh for the optical calculations that has cells approximately equal in size to those of the CFD mesh; however, the optical mesh is aligned with the direction of signal propagation. For this study, the beams radiate outwards (vertically) from the wall. The densities from the fluid simulations are linearly interpolated onto the optical mesh. The index of refraction is integrated along the path of signal propagation to obtain the total OPL. The spatially averaged OPL is then subtracted and the result is the OPD. The current method for calculating optical aberrations is not tightly coupled to the flow field calculations; solutions in this simulation are obtained at specific times.

IV. Conditions of Numerical Simulations

The numerical simulation conditions are presented in two sections. Section IV A discusses the simulation parameters for each portion of the study. Section IV B discusses the grids used in the analyses.

A. Flow Parameters/Geometry

The simulations in this study are conducted for a turbulent Mach 4 flow over a flat plate. The flat plate extends in the streamwise direction to approximately 0.64 m. The cases, for both real and perfect gases, are run with the free stream conditions described in Table 2.

Table 2. Turbulence Study Flow Parameters[2]

Parameter	Value
M_∞	4
ρ_∞	0.5 kg/m^3
T_∞	5000 K
Y_{O2}	0.0166
Y_{N2}	0.616
Y_{NO}	0.0501
Y_N	0.00890
Y_O	0.309

An adiabatic wall condition is utilized. The free stream mass fractions are set to their equilibrium values at the freestream values of density and temperature. These conditions are representative of those behind the oblique shock wave formed by a 26 degree wedge flying at Mach 20 at 20 km in altitude. Free stream conditions ensure appropriate physics are obtained.[2]

B. Grid Structure

The ILES mesh is created to have $\Delta x+ = 15$, $\Delta z+ = 25$, and $\Delta y+ = 0.14$. These values are deemed sufficiently refined for an ILES simulation following guidelines outlined in Ref. [14]. The mesh is three-dimensional to obtain physical results since turbulence involves inherently three dimensional phenomena. The size of the domain in the Cartesian *z* dimension (spanwise) is 0.1475 m.

The mesh is divided vertically into three regions (denoted in red); see Fig. 1. The first consists of a *y*+ of 0.14 at the wall stretching to a *y*+ of 28.

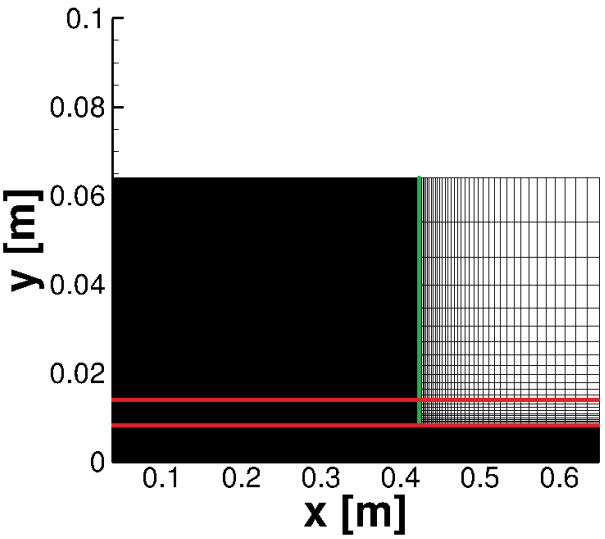

Figure 1. Mesh structure

The second region has equal spacing and extends to the point at which 1.4 times the expected boundary layer at the exit plane is reached. The third region is then stretched to the top boundary. The grid is also split into two horizontal regions (denoted in green in Fig. 1). The first consists of uniform spacing and begins at the front of the plate and extends to *x*= 0.4 m. After *x*=0.4 m the grid is stretched to *x*=0.6 m.

V. Results

The results are divided into three sections. The first section presents a general assessment of the Mach 4 perfect and real gas flows over the flat plate. This section emphasizes features that are important to optical assessments. The second section presents how nonequilibrium phenomena affect the flow. The influence of these features on optical distortion is presented in the third section. It should be noted that the data presented is taken at 0.25 ms for both the real and perfect gas cases.

A. Flow Field

Figure 2 presents the temperature profiles of (A.) the perfect gas flow and (B.) the real gas flow for Mach 4 flow over the flat plate. The data is extracted from a plane at z=0.077 m. Both flows are characteristic of a high speed turbulent flow over a flat plate. There is a thin fluctuating boundary layer confined in the region near the wall. The temperature at the wall reaches approximately 18000 K in the perfect gas simulations and 7500 K in the real gas simulation. The resultant difference in temperature is caused by the inclusion of the high temperature real gas effects in (B.). Endothermic reactions drain energy that would otherwise be in the translational and rotational mode (as it is in the perfect gas flow).

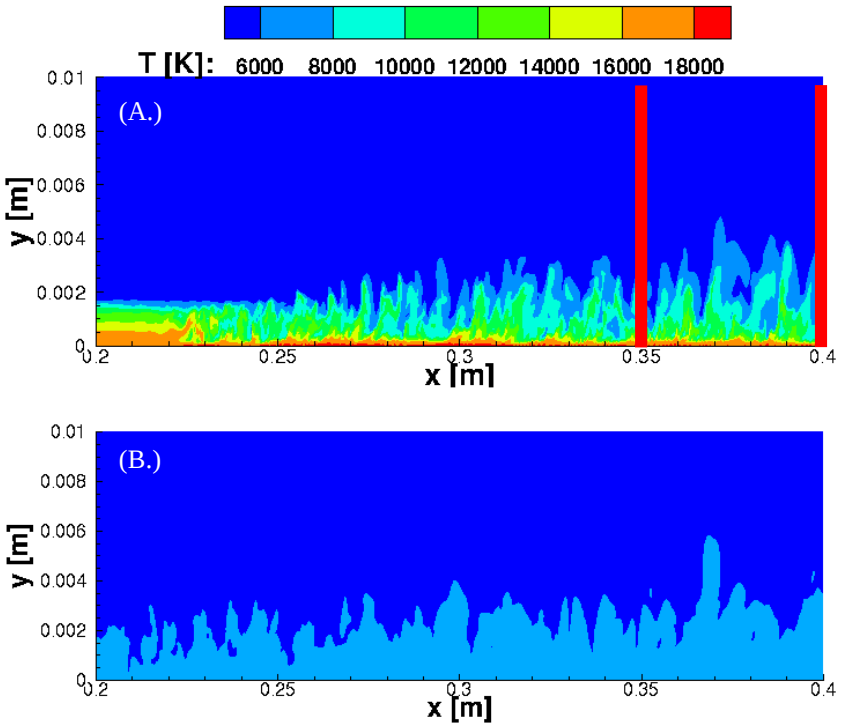

Figure 2. Temperature contours for (A.) perfect gas flow and (B.) real gas flow

It should be noted that the entire computational domain is not shown in Fig. 2; instead, the area in the fully turbulent regime (for the nonequilibrium simulation) is illustrated. The domain utilized for the optical calculations extends from x=0.35 meters to x=0.4meters and is noted in Fig. 2 (A.). This domain is assessed because of its distance from the transition location in both simulations and the coinciding need to minimize effects produced by these transitions to turbulent flow.

Figure 3 presents the density contours for the flow over the flat plate for the perfect gas (A.) and the real gas (B.) simulations, respectively. Again, the figure illustrates that both flows are typical of a high speed, high Reynolds number flow over a flat plate. Due to the high temperature caused by the adiabatic wall, we see in Fig. 3 that the density decreases near the wall. The decrease is more significant for the perfect gas flow, which is consistent with the equation of state.

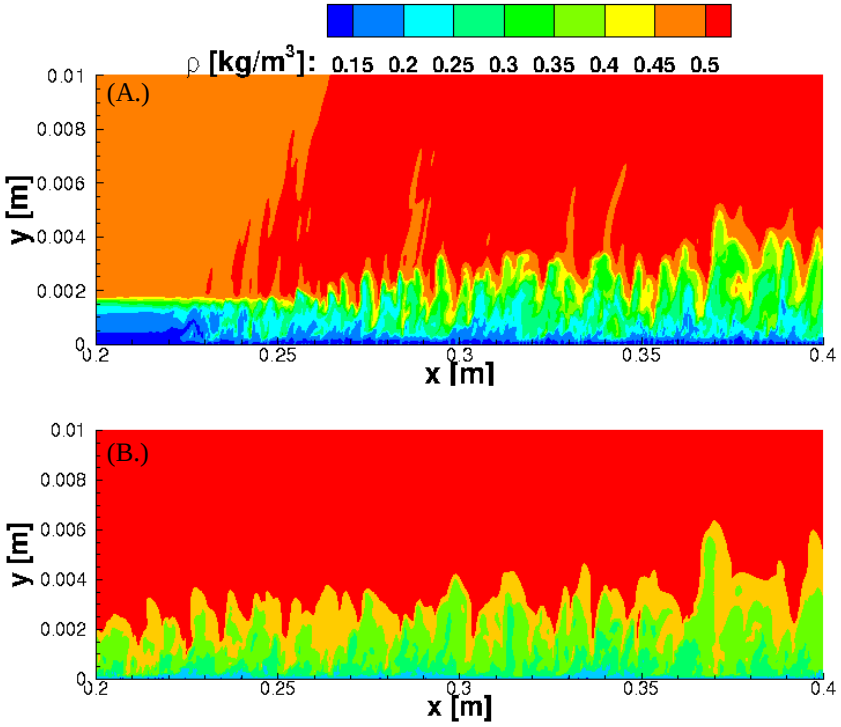

Figure 3. Density contours for (A.) Perfect Gas and (B.) Real Gas

We may also note that the real gas flow transitions to fully developed turbulence at a shorter distance along the plate than the perfect gas flow transitions. The real gas trip mechanism, which has the same strength as the perfect gas trip, is imposed on a field that has multiple energy modes (translational-rotational, vibrational, and chemical). The total energy is divided amongst these energy modes in the real gas case (unlike the perfect gas, which has only the translational and rotational modes which are in equilibrium). The higher translational energy of the perfect gas flow pushes the transition location downstream. In both cases, once the turbulence has fully developed, the density fluctuates within the boundary layer, as expected with turbulent flows.

Figure 4 presents the vertical density profiles extracted at x=0.35 m (the beginning of the zone used for optical assessment).

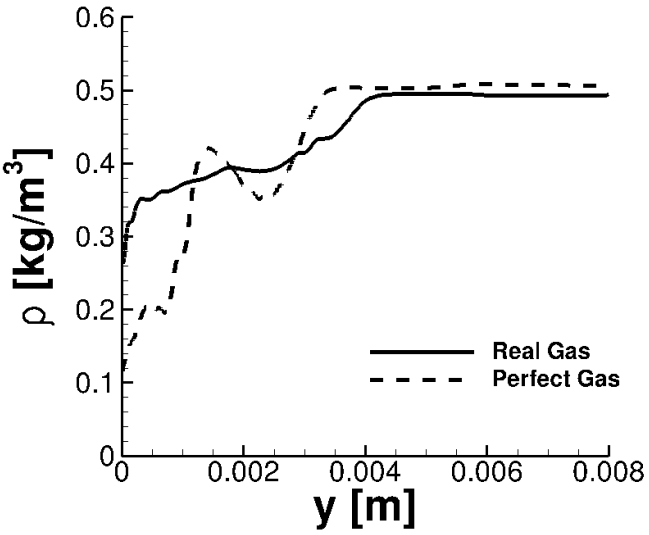

Figure 4. Density profile at x=0.35 m

Figure 4 better illustrates the relatively low density at the wall for the higher temperature, perfect gas simulation. The density at the wall is 54.5% lower for the perfect gas case.

Figure 5 shows the skin friction coefficient for the real and perfect gas cases along the plate for a plane at z=0.077 m. The skin friction upstream of 0.2 m for the perfect gas and near zero for the real gas is lower, which is indicative of laminar flow. At approximately 0.2 m for the perfect gas and 0.01 m for the nonequilibrium gas case, the skin friction coefficient increases sharply. This increase is caused by the transition to turbulence. The skin friction coefficient remains high throughout the turbulent regime.

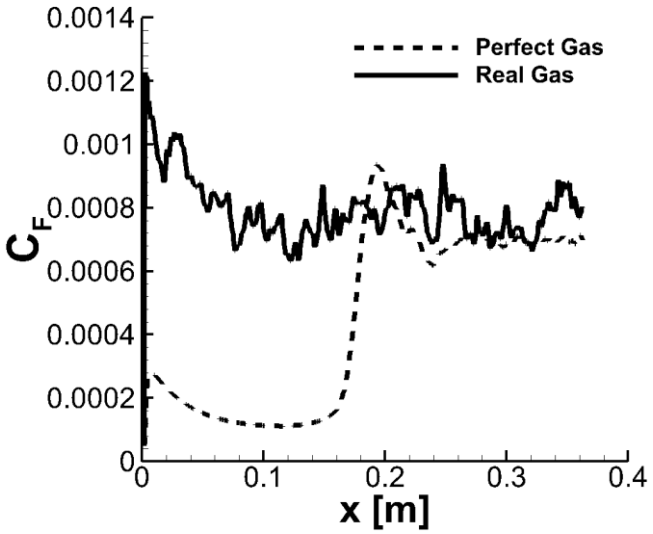

Figure 5. Skin friction coefficient

Figure 5 reinforces the conclusion drawn from Fig. 3, that the nonequilibrium real gas flow transitions closer to the imposed vortices than the perfect gas simulation.

In order to verify the simulations, Fig. 6 shows non-dimensional velocity profiles in the boundary layers. The profiles obtained from the simulations are each compared to the Van Driest theoretical law of the wall.[25] The velocity and distance from the wall (Cartesian y) are non-dimensionalized as illustrated below.

$$y+= \frac{yu_\tau}{\nu} \ , u_\tau = \sqrt{\left(\frac{\tau_w}{\rho}\right)} \quad and \quad u^+ = \frac{u}{u_\tau} \tag{15}$$

where τ_w is shear stress at the wall. Also plotted in the figures is the correlation for the viscous sublayer.

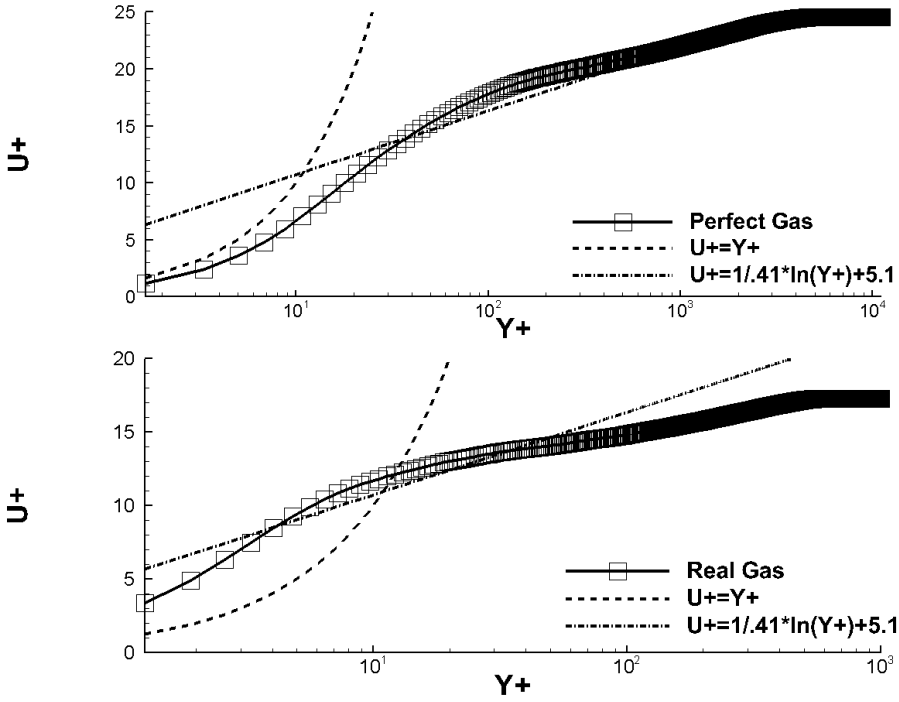

Figure 6. Velocity profiles for perfect and real gas compared to theoretical curves

The results for the perfect gas flow are in good agreement with theory. The differences in the real gas velocity profiles (from theory) can be attributed to the derivation of the law of the wall which did not consider compression or nonequilibrium effects.

To further assure that the appropriate data is acquired for optical calculations, progressive averages are monitored for the conserved variables. The cumulative moving average for the turbulent kinetic energy (TKE) for the perfect gas and real gas simulations, respectively, at a location near the wall (in dimensional coordinates x=0.35 m, y=0.001 m, and z=0.0077 m) is shown in Fig. 7. The progressive averages are observed at multiple locations, and the same temporal evolutions are obtained.

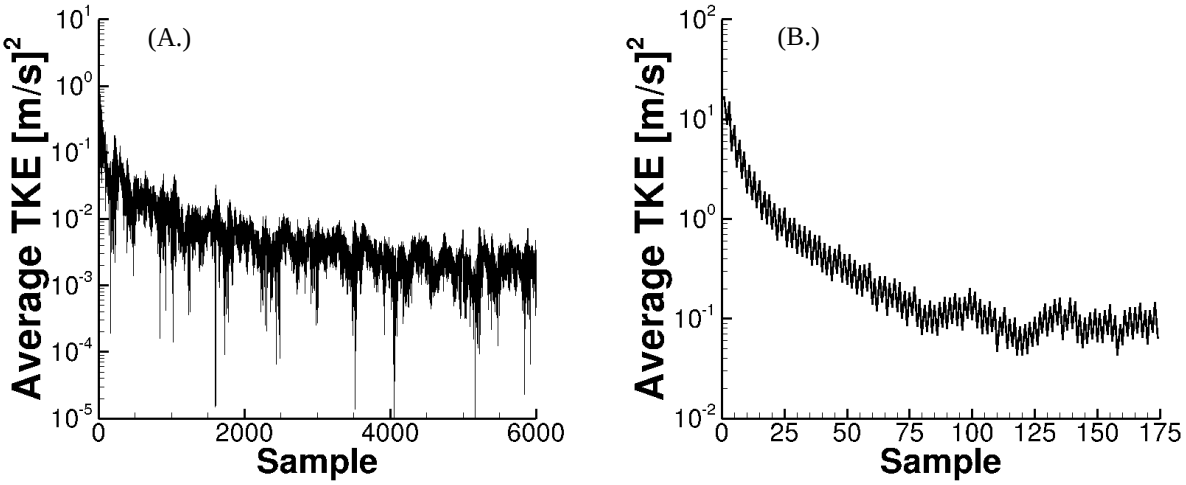

Figure 7. Cumulative moving average of TKE for (A.) Perfect Gas and (B.) Real Gas

At approximately 4000 samples and 100 samples for the perfect gas and real gas simulations, respectively, the progressive averages plateau which indicates the transients in the flow have diminished. The turbulence took longer to establish in the perfect gas flow due to the high translational energy.

B. Nonequilibrium Features

As briefly mentioned in section V A., the nonequilibrium features of the real gas flow can drastically alter the properties associated with that flow. To better understand these real gas features, the thermal nonequilibrium associated with this flow is assessed.

At the high temperatures present in the flow, the vibrational mode of energy can becomes excited. It may not always be possible for the vibrational energy to stay in equilibrium with the translational mode. This appears in the flow as a difference between the translational and vibrational temperatures. In the near wall region, the translational temperature is only approximately 10 K higher than the vibrational temperature, suggesting that very little energy is required to transfer into the vibrational mode in order to bring the flow to equilibrium. While there are differences present in the temperatures, these differences are very slight. This implies that the energy transfer into the vibrational mode does not play a large role in this particular flow. The lack of thermal non-equilibrium can be attributed to the high pressures in the flow (approximately 8 atm) which promote energy exchanging collisions and consequently quickly pushes the flow towards thermal equilibrium.

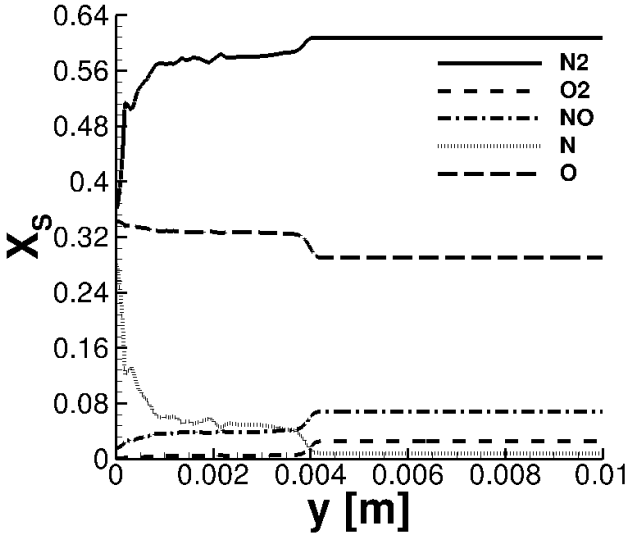

Figure 8. Mass fraction profiles (z=0.0077 m, x=0.35 m)

Besides energy transferring into the vibrational mode, nonequilibrium air flow often experiences energy being absorbed by the dissociation of the diatomic species, N_2 and O_2. The result of this phenomenon is mass fraction profiles that vary throughout the computational domain. Figure 8 shows the mass fraction profiles of the 5-species in air taken from the real gas solution at x=0.35 m and z=0.077 m. Near the hot wall, the fraction of diatomic nitrogen decreases as the wall is hot enough to promote significant nitrogen dissociation. Large changes in the concentration of diatomic and monatomic oxygen are not observed. This is because the free stream temperature is already high enough to support oxygen dissociation. Near the wall the mass fraction of NO decreases; there is enough energy near the wall to support NO dissociation. These mass fractions modify the index of refraction; see Eqns. (11) and (12).

The various energy exchanges that occur in nonequilibrium flows have an effect on the turbulent fluctuations. Figure 9 shows the density fluctuations at x=0.35 m and z=0.077 m, which are up to 89.9% smaller for the real gas simulation.

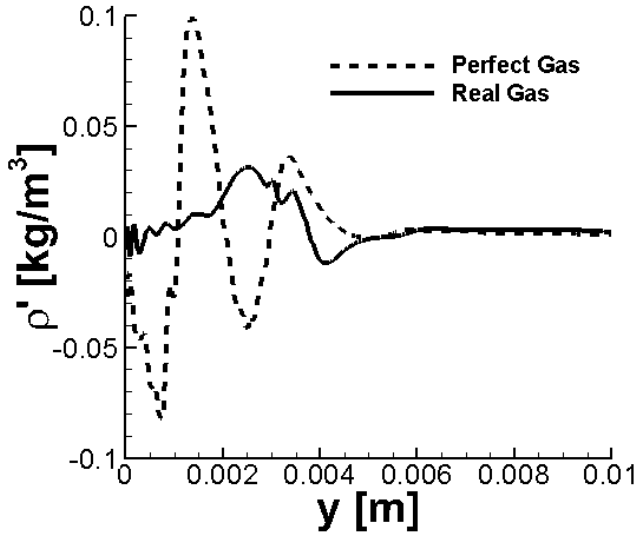

Figure 9. Density fluctuations of perfect and real gas (z=0.0077 m, x=0.35 m)

This supports the conjecture proposed by Martin that energy is taken from the turbulent kinetic energy and transferred into the chemical energy modes.[2] The density fluctuations are shown because of their large influence on the optical properties of the flow via Eqn. (11). As the equations suggest, the more varied the density profiles are, the larger the variation in optical path lengths/differences are (which are used to describe the phase shift for a beam traversing a flow field).

C. Optical Distortion

Figure 10 shows the profiles of index of refraction obtained by applying Eqns. (11) and (12) to the perfect gas and real gas density profiles at x=0.35 m and z=0.0077 m. It should be noted that for the perfect gas simulations, a single Gladstone-Dale constant is utilized. A Gladstone-Dale profile is used for the nonequilibrium simulation, as the mass fractions vary throughout the field in the real gas simulation. The index of refraction largely follows the trends of the overall density profiles shown in Fig. 4 with minor modifications due to species concentrations (in the real gas flow). The difference between the real gas and perfect gas indices of refraction is 45% which is similar to the percent difference in the density at the wall.

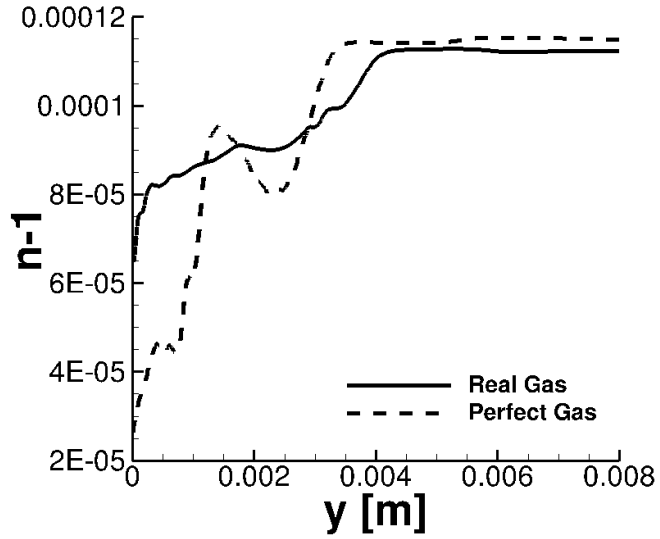

Figure 10. Index of refraction profile

All of the refraction index profiles like the example in Fig. 10 are integrated, and the resulting OPDs are obtained. Figure 11 depicts the optical distortion calculated in a plane where *z* is equal to 0.077 m and *x* is as shown in Fig. 2 (A.). There is more variation from the mean optical path length for the perfect gas simulation. This can be attributed to the larger fluctuations in density (see Fig. 10) that are present in the perfect gas simulation. The fluctuations in the Gladstone-Dale constant caused from the varying mass species in the real gas simulation are not the dominant contributor to the index of refraction.

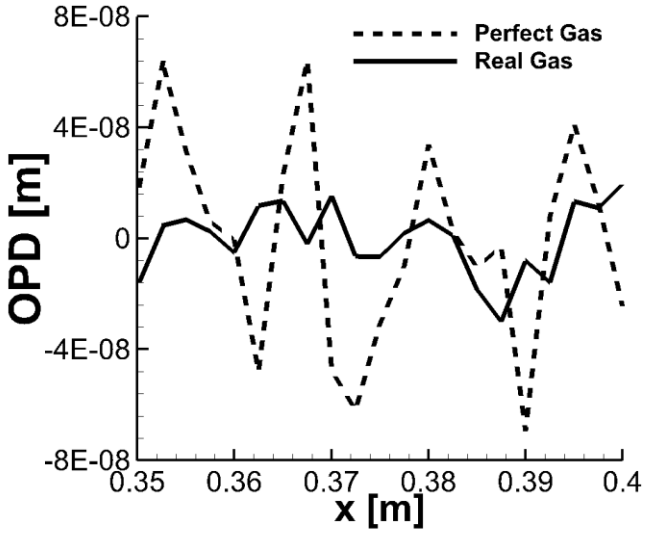

Figure 11. Optical path distortion

The root mean square (RMS) value of OPD for the perfect gas is 66.0% larger than that for the real gas at the plane utilized in this study. There is larger variation in the optical lengths for the perfect gas case. Various other times and planes are analyzed for the optical portion of the study and though the positions of the peaks and troughs shift, the RMS magnitude of the fluctuations remains approximately constant at each location, independent of time.

VI. Conclusion

For vehicles traveling at hypersonic speeds it is imperative to consider flow phenomena that differ from those involved at lower speeds. For example, thermochemical nonequilibrium effects can become important as Mach number increases above 5, and may couple into defining the characteristics of the turbulent boundary layer. This study examined various aspects of a turbulent hypersonic flow and determined the optical distortion a beam would experience as it traverses such a field.

A flat plate simulation was conducted to determine the effects of resolved hypersonic turbulence on aero-optical properties. The simulation was conducted at Mach 4 over an adiabatic wall with a free stream density of 0.5 kg/m^3, and a free stream temperature of 5000 K which is representative of the post shock conditions of a wedge flying at Mach 20 at an altitude of 20 km. Optical calculations were performed on each flow using the Gladstone-Dale relation. The flow fields, obtained with both perfect and real gas assumptions, produced non-linear OPD profiles, characteristic of turbulent flow. Furthermore, the perfect gas OPD was on average 66.0% larger than the real gas OPD. This is caused by the larger fluctuations in density experienced by the perfect gas flow (due to the relatively higher energy in the translational mode when compared to the real gas flow). The results presented suggest that capturing the features of resolved turbulence and thermochemical nonequilibrium is important for aero-optical calculations. For the conditions studied, if nonequilibrium flow phenomena were to be neglected the optical distortion would be over-predicted.

Future work will include simulations with more realistic flow conditions that employ higher fidelity nonequilibrium models.

Acknowledgments

The first two authors acknowledge funding through a grant from the Air Force Research Laboratory, monitored by Eswar Josyula. The second two authors would like to acknowledge the Air Force Research Laboratory (M. S. Brown, AFRL/RQHF and I. A. Leyva, AFOSR) for their support. This study was completed, in part, on AFRL's high performance computing system. L. Mackey would also like to express her gratitude to N. Bisek and R. Gosse of AFRL for the many useful conversations regarding turbulence and the use of computational resources.

References

[1]Gladstone, J. H. and Dale, T. P., "Researches on the refraction, dispersion and sensitiveness of liquids," Phil. Trans. Royal Soc. London 153, 1864, pp.317–343.

[2]Martin, M.P., "Exploratory Studies of Turbulence.Chemistry Interactions in Hypersonic Flows," AIAA Paper 03-4055, 2003.

[3]Duan, L., and Martin, M.P., "Effect of Finite-Rate Chemical Reactions on Turbulence in Hypersonic Turbulent Boundary Layers," AIAA paper 2009-588, 2009.

[4]Neville, A.G., Nompelis, I., Subbareddy, P. K., and Candler, G.V., "Effects of Thermal Non-equilibrium on Decaying Isotropic Turbulence," AIAA Paper 2014-3204, 2014.

[5]Weng, M., Mani, A., and Stanislav, G., "Physics and Computation of Aero-Optics," Annual Review of Fluid Mechanics, Vol. 44, 2012, pp.299-321.

[6]J.S. Jewell and R.L. Kimmel. "Boundary Layer Stability Analysis for Stetson's Mach 6 Blunt Cone Experiments." Journal of Spacecraft and Rockets, Vol. 54, No. 1, pp. 258-265, 2017. DOI: 10.2514/1.A33619.

[7]Subbareddy, P.K., and Candler, G.V., "DNS of Transition to Turbulence in a Mach 6 Boundary Layer," AIAA paper 2012-3106, 2012.

[8]Anderson, J. D., Hypersonic and High Temperature Gas Dynamics, 1st Edition, McGraw-Hill, 1989.

[9]Boyd, I. D. and Schwartzentruber, T. E., Nonequilibrium Gas Dynamics and Molecular Simulation, 1st Edition, Cambridge University Press, 2017.

[10]Park,C., "Calculation of Real-Gas Effects on Blunt-Body Trim Angles," AIAA Journal, Vol. 30, No. 4, 1992, pp. 999–1006

[11]Park, C. *Nonequilibrium Hypersonic Aerothermodynamics*, John Wiley & Sons, 1990.

[12]Park, C., "The Limits of Two-Temperature Model," AIAA Paper 2010-911, January 2010.

[13]Landau, L., and Teller, E., "Zur Theorie der Schalldispersion," Physikalische Zeitschrift der Sowjetunion, Vol, 10, 1936, pp. 34-43.

[14]Millikan, R.C., and White, D.R., "Systematics of Vibrational Relaxation," Journal of Chemical Physics, Vol. 39, 1963, pp. 3209-3213.

[15]Alpher, R.A., and White, D.R., "Optical Refractivity of High Temperature Gases. I. Effects Resulting from Dissociation of Diatomic Gases," Physics of Fluids, Vol.153, 1958.

[16]Merzkirch, W., *Flow Visualization*, 2nd edition, Elsevier, 2012.

[17]Anderson, J. H. B.,"An Experimental Determination of the Gladstone-Dale Constants For Dissociating Oxygen," Technical note, 1967.

[18]Wolfe, W. E. and Zissis, G. J., *The Infrared Handbook,* 4th Edition, IRIA Series in Infrared and Electro-Optics, 1993.

[19]Vogiatzis, K., Josyula, E., and Vedula, P., "Role of High Fidelity Nonequilibrium Modeling in Laminar and Turbulent Flows for High Speed ISR Missions," AIAA paper 2016-4317, 2016.

[20]Wyckham, C. and Smits, A. 2009 Aero-optic distortions in transonic and hypersonic turbulent boundary layers. AIAA J. 47 (9), 2158-2168.

[21]JingYuan, L., "A three-equation turbulence model for high-speed flows," Science China. Vol.56, No.803-811, April 2013.

[22]Gordeyev, S., Smith, A., Cress, J., and Jumper, E. 2014 Experimental studies of aero-optical properties of subsonic turbulent boundary layers. J. Fluid Mech. 740, 214-253.

[23]S. Gordeyev, R.M. Rennie, A.B. Cain, and T.E. Hayden. Aero-Optical Measurements of High-Mach Supersonic Boundary Layers. AIAA Paper 2015-3246, 2015.

[24]Yanta, W. J., Spring, W. C., III, Lafferty, J. F., Collier, S. C., Bell, R. L., Neal, D., Hamrick, D., Copland, J., Pezzaniti, L., Banish, M., and Shaw, R., "Near-and Far-Field Measurements of Aero-Optical Effects due to Propagation Through Hypersonic Flows," AIAA Paper 2000- 2357, 2000.

[25]E. R. Van Driest, "On turbulent flow near a wall," J. Aeronaut. Sci., 23, No. 11, 1007-1011 (1956).

[26]Wright, M. J., Candler, G. V., and Bose, D., "Data-parallel line relaxation method for the Navier-Stokes equations," AIAA Journal, Vol. 36, No. 9, 1998, pp. 1603-1609.

[27]J.S. Jewell. *Boundary-Layer Transition on a Slender Cone in Hypervelocity Flow with Real Gas Effects*. Ph.D. Thesis. California Institute of Technology, Pasadena, CA. 2014. DOI: 10.7907/Z9H9935V.

[28]J.S. Jewell and R.L. Kimmel. "Boundary Layer Stability Analysis for Stetson's Mach 6 Blunt Cone Experiments." Journal of Spacecraft and Rockets, Vol. 54, No. 1, pp. 258-265, 2017. DOI: 10.2514/1.A33619